

LA-UR- 01-4433

Approved for public release;  
distribution is unlimited.

Title: Low Frequency Electrostatic Instability in a Helicon Plasma

Author(s): Max Light, Francis F. Chen, and P.L. Colestock

Submitted to: Physics of Plasmas



## Los Alamos

NATIONAL LABORATORY

Los Alamos National Laboratory, an affirmative action/equal opportunity employer, is operated by the University of California for the U.S. Department of Energy under contract W-7405-ENG-36. By acceptance of this article, the publisher recognizes that the U.S. Government retains a nonexclusive, royalty-free license to publish or reproduce the published form of this contribution, or to allow others to do so, for U.S. Government purposes. Los Alamos National Laboratory requests that the publisher identify this article as work performed under the auspices of the U.S. Department of Energy. Los Alamos National Laboratory strongly supports academic freedom and a researcher's right to publish; as an institution, however, the Laboratory does not endorse the viewpoint of a publication or guarantee its technical correctness.

# Low Frequency Electrostatic Instability in a Helicon Plasma

Max Light

*Los Alamos National Laboratory, Los Alamos, New Mexico 87545*

Francis F. Chen

*Electrical Engineering Department, University of California, Los Angeles, California 90095-1594*

P. L. Colestock

*Los Alamos National Laboratory, Los Alamos, New Mexico 87545*

(July 26, 2001)

## Abstract

Recent discoveries in a helicon plasma show a decrease in equilibrium plasma density as magnetic field strength is increased. This can be explained in the framework of a low frequency electrostatic instability. However, quiescent plasma behavior in helicon sources has been hitherto accepted. To verify the existence of an instability, extensive measurements of fluctuating quantities and losses as a function of magnetic field were implemented. Furthermore, a theoretical model was developed to compare to the measurements. Theory and measurement show very good agreement; both verifying the existence of a low frequency instability and showing that it is indeed responsible for the observed density characteristic.

## I. INTRODUCTION

Interest in the helicon plasma discharge source continues to be strong in view of its applicability to industrial needs, as a tool to study basic plasma physics, and even as a means for spacecraft propulsion [1–6]. The physics of the helicon wave, a radially bounded whistler, have been studied extensively in these sources [7–9]. Equilibrium plasma behavior and loss scaling with magnetic field, however, have not received a great deal of attention because it has been generally accepted that a quiescent plasma can be produced. Recent reports [10–14] of the plasma density  $n_0$  dropping off with increased magnetic field strength  $B_0$ , as shown in Figure 1, require a new perspective on the assumed quiescent plasma behavior.

The basic equilibrium loss mechanisms can be treated separately as perpendicular and parallel to the magnetic field for the purpose of this examination. However, in general they can not be de-coupled. Along the magnetic field the ions control the loss rate and are assumed to escape across the end sheaths at the sound speed [15]. This gives a parallel flux (neglecting density gradients) that scales linearly with density

$$\Gamma_{||} = n_0 C_s \quad (1)$$

where  $C_s$  is the ion sound speed. Perpendicular to the magnetic field direction [16], the flux is given as a Fick's law

$$\Gamma_{\perp} = -D_{\perp} \nabla_{\perp} n_0 \quad (2)$$

where the perpendicular diffusion coefficient,  $D_{\perp}$ , is a function of collision rate and magnetic field strength. The dependence of  $D_{\perp}$  goes as  $1/B_0^2$  for both coulomb and neutral collisions. Bohm [17], experimentally found that for coulomb collision dominated plasmas,  $D_{\perp}$  actually goes as  $1/B_0$ . In any case, perpendicular diffusion, and hence radial flux, goes, at worst, as the inverse of the magnetic field strength.

The perpendicular and parallel loss times in a cylindrical chamber due to the above mechanisms can be simply estimated. They are given as

$$\tau_{\perp} = \frac{R^2}{D_{\perp}} \quad \tau_{\parallel} = \frac{L/2}{C_s} \quad (3)$$

where  $R$  is the chamber radius and  $L$  its length. Assuming Bohm diffusion and using  $B_0 = 900G$ ,  $T_e = 4eV$ , and  $n_0 = 10^{13}/cm^{-3}$  (the parameters corresponding to the maximum density with neon in this experiment) reveals

$$\tau_{\perp, Bohm} = 2mS \quad \tau_{\parallel} = 0.2mS$$

showing that axial diffusion should, in theory, dominate for this experiment. Axial losses scale as  $n_0$  and show no direct correlation with magnetic field strength. On the other hand, radial losses scale as (worst case)  $1/B_0$ , which is in the wrong direction to account for the observed  $n_0(B_0)$  behavior.

One possible mechanism for enhanced plasma loss across the magnetic field is the  $E \times B$  velocity imparted to plasma particles from azimuthal electric field fluctuations due to a low frequency electrostatic instability [18–21]. This gives rise to what is sometimes called “anomalous” radial diffusion and can greatly affect the equilibrium plasma. Instabilities of this kind can be driven by a gradient in equilibrium density, such as the resistive drift wave [22–29], or a gradient in equilibrium space potential profile, for instance the Kelvin-Helmholtz [30–33] or Simon-Hoh [34,35] instabilities.

This was not initially anticipated in the present plasma discharge due mainly to the fact that low frequency oscillations had never before been observed in the usual operating regimes. They were initially reported as a nuisance during measurements of the helicon magnetic field components [36]. The detection frequency of a few  $MHz$  was observed to have a low frequency modulation of a few  $KHz$ , rendering measurements of the wave magnetic field components useless at certain magnetic field strengths. This is shown in Figure 2. Figure 16 shows that the observed saturation in  $n_0(B_0)$  corresponds with the onset of strong low frequency fluctuations in ion saturation current as well. Normalized density fluctuations,  $\tilde{n}/n_0$ , were greater than 10 percent in the region where  $n_0(B_0)$  began to significantly deviate from a monotonically increasing characteristic. These results suggested an interpretation of

the detected density and potential fluctuations in the equilibrium plasma as the result of an instability.

## II. THEORY

The instability model was based on a normal mode, or linear, analysis to predict the instability characteristics as a function of magnetic field strength. In this approach ion and electron density and velocity, and plasma potential are expanded to first order about an equilibrium state in order to characterize the behavior of (first order) fluctuating quantities [38]. This description is good for predicting onset and growth up to the nonlinear regime; however, it can say nothing about saturation behavior.

The instability was assumed to be absolute, since it was observed to grow at all points in the plasma with time. Thus, the wavenumber  $k$  was assigned to be real and the eigenfrequency  $\omega$  complex. Directionality of growth and damping is therefore unambiguous.

To reach the dispersion relation, the linearized velocities are solved as functions of potential from the force equations and coupled into their respective continuity equations. For low frequency electrostatic perturbations, the plasma approximation  $n_i = n_e$  is sufficient to close the set of equations.

To clarify the situation, the assumptions imposed on the linear model are:

- A two fluid description is used. This facilitates the interpretation of “slippage” between the electron and ion fluids.
- For the experimental parameters in the present work, neutral collisions dominate coulomb collisions by at least an order of magnitude [38,39].
- Ions are “cold”:  $T_i = 0, T_e \neq 0$  Finite temperature ions will not affect the results of this theory because the collision term dominates the pressure term in the ion momentum equation both in equilibrium and perturbation.
- Electron inertia is ignored:  $m_e/M_i = 0$ .

- Fluctuations are electrostatic. This is accurate for low  $\beta$  plasmas (as in the present case) where there is no significant magnetic field from the wave. This also implies  $\omega/k_{\parallel} \ll V_A$ , where  $V_A$  is the Alfven speed, and the plasma approximation is therefore valid.
- No resonant particles:  $V_{th,i} \ll \omega/k_{\parallel} \ll V_{th,e}$ . Ions, while they could have a thermal velocity near the wave phase velocity, are too collisional to become resonant with the wave.
- Fluctuating quantities will have a Fourier representation. For example,  $\vec{v} = V(r)e^{i(m\theta+k_z z-\omega t)}$  in cylindrical geometry where the inhomogeneity exists in the radial direction.
- An equilibrium radial electric field exists. This is based on experimental measurements and thus the potential will have both zero and first order components:  $\phi(r) = \phi_0(r) + \tilde{\phi}(r, \theta, z)$ .

Consider a radially bounded plasma in a cylindrical geometry immersed in an axial magnetic field. The field magnitude will be constant across the radius of the plasma. Density and potential will have only radial variations. The equations governing this situation for each species are the momentum equation for ions

$$M_i n_i \left( \frac{\partial \vec{V}_i}{\partial t} + \vec{V}_i \cdot \nabla \vec{V}_i \right) = e n_i \left( -\nabla \phi + \vec{V}_i \times \vec{B}_0 \right) - M_i n_i \nu_{ci} \vec{V}_i \quad (4)$$

the momentum equation for electrons

$$0 = -e n_e \left( -\nabla \phi + \vec{V}_e \times \vec{B}_0 \right) - K T_e \nabla n_e - m_e n_e \nu_{ce} \vec{V}_e \quad (5)$$

and continuity for each species

$$\frac{\partial n_j}{\partial t} + \nabla \cdot (n_j \vec{V}_j) = 0 \quad (6)$$

which, as specified earlier, are closed with the plasma approximation.

## A. Equilibrium Velocities

In this section, the zero subscript will be dropped and axial zero-order velocities will be neglected for both species (beam-plasma effects were ignored).

### 1. Ion Equilibrium

Taking the  $\hat{r}$  component of Equation 4 gives insight into both the convective derivative and perpendicular collision contributions to the ions' motion

$$\frac{v_r v_r'}{\Omega_c} - \frac{1}{r} \frac{v_\theta^2}{\Omega_c} = -\frac{\phi'}{B} + v_\theta - \frac{\nu_{ci}}{\Omega_c} v_r \quad (7)$$

where  $'$  denotes  $\partial/\partial r$ ,  $\Omega_c = eB/M_i$  is the ion cyclotron frequency, and  $\nu_{ci}$  represents the ion-neutral collision frequency. The left hand side of Equation 7 represents the contribution of the convective derivative to the ion motion, which introduces a new term along with the  $E \times B$  drift term and a collisional part. For parameters in the regime of the plasma in this experiment, the third term on the right and first term on the left of Equation 7 can be neglected. To understand why, first note that the only force acting on the ions is radially directed in the form of the electric field [ $\vec{E} = E(r) = -\nabla\phi(r)$ ]. This gives the ions a  $\theta$  component to their guiding center velocity from the general relation [16]

$$\vec{v}_F = \frac{1}{q} \frac{\vec{F} \times \vec{B}}{B^2} \quad (8)$$

The only mechanism which can impart a radial component to their guiding center velocity is due to collisions in a diffusion process (the third term on the right of Equation 7) which can be written as

$$v_r \sim \left( \frac{\mu}{1 + \Omega_c^2/\nu_{ci}^2} \right) \nabla\phi - \left( \frac{D}{1 + \Omega_c^2/\nu_{ci}^2} \right) \frac{\nabla n}{n} \quad (9)$$

where  $\mu$  and  $D$  are the mobility and diffusion coefficients respectively, written as

$$\mu = \frac{|q|}{M_i \nu_{ci}} \quad D = \frac{KT_i}{M_i \nu_{ci}} \quad (10)$$

and  $\Omega_c^2/\nu_{ci}^2 \gg 1$ . Ions are assumed to be cold. In fact, the ions are most likely at room temperature so that  $D$  is extremely small. Using this and the definition of  $\mu$  above, the radial velocity component can be reduced to

$$v_r \sim \frac{\phi'}{B} \frac{\nu}{\Omega_c} \quad (11)$$

which is the familiar  $E \times B$  drift (but in the radial direction) reduced by the ratio  $\nu/\Omega_c$ . So, in fact, the first term on the left and third term on the right of Equation 7 go as  $\Omega_c^{-2}$ . In this experiment,  $\Omega_c \sim 10^6$  /sec and  $\nu_{ci} \sim 10^3$  /sec so that the two terms mentioned above can be neglected with no effect on the outcome of the ion equilibrium velocity. Thus, in equilibrium, the radial velocity component can be neglected and perpendicular collisions play an insignificant role in the ion equilibrium velocity terms.

Equation 7 can now be reduced to

$$-\frac{1}{r\Omega_c}v_\theta^2 = -\frac{\phi'}{B} + v_\theta \quad (12)$$

which consists of the  $E \times B$  guiding center drift and a centrifugal force term from the convective derivative. Solving the quadratic for  $v_\theta$  and picking the root that gives zero velocity in the limit of no electric field ( $\phi' \rightarrow 0$ ) gives an expression for the ion equilibrium velocity

$$v_\theta = -\frac{r\Omega_c}{2} \left( 1 - \sqrt{1 - 4\frac{\phi'}{B} \frac{1}{r\Omega_c}} \right) \quad (13)$$

This can be further reduced by closer examination of the expression under the radical revealing a condition on the radial electric field for a stable equilibrium solution

$$E < \frac{1}{4}Br\Omega_c \quad (14)$$

In fact, from experimental measurements

$$E \ll \frac{1}{4}Br\Omega_c$$

allowing a binomial expansion on the radical term in Equation 13 such that

$$v_\theta = \frac{\phi'}{B} \quad (15)$$

So the equilibrium velocity for the ions is simply the  $E \times B$  guiding center drift  $v_{EB}$ . It can be argued that, near the origin, the  $1/r$  dependence in Equation 13 could dominate. However, the dependence of  $\phi'$  at that location must also be taken in to account. In particular, it is likely that  $\phi'/r$  cancels this at  $r = 0$ . If not, the theoretical model for  $\phi(r)$  can be chosen to make it so.

## 2. Electron Equilibrium

Coupling the  $\theta$  component into the  $r$  component in Equation 5 gives an expression for  $v_\theta$

$$v_\theta \left( 1 - \frac{\nu_{ce}^2}{\omega_c^2} \right) = \frac{\phi'}{B} - \frac{KT_e}{eB} \frac{n'}{n} \quad (16)$$

where  $\nu_{ce}$  is now the electron-neutral collision rate and  $\omega_c$  is the electron cyclotron frequency. Again, typical values for  $\nu_{ce}$  and  $\omega_c$  are  $10^8/sec$  and  $10^{10}/sec$  respectively allowing the  $\nu_{ce}^2/\omega_c^2$  term on the left hand side of Equation 16 to be dropped. This reduces the equilibrium electron velocity to

$$v_\theta = \frac{\phi'}{B} - \frac{KT_e}{eB} \frac{n'}{n} \quad (17)$$

$$= v_{EB} - v_D \quad (18)$$

The second term in Equation 17 is the well known diamagnetic drift velocity due to electron pressure,  $KT_e \nabla n$ .

The equilibrium guiding center velocities for both species are perpendicular to the magnetic field and, in fact, only in the  $\theta$  direction. Radial guiding center velocity components are due to diffusive processes which were neglected because of the magnetic field. This is equivalent to ignoring cross field diffusion for the equilibrium state because this process occurs on a timescale orders of magnitude greater than any of the derived equilibrium azimuthal motions. This is not to be confused with radial flow due to the instability mechanism which will occur on the same timescale as the equilibrium motions.

## B. Perturbation Description in Slab Geometry

The slab model is a good starting point to describe the instability. Making the plane-wave approximation and assuming a local wavenumber  $k_x$  in the direction of plasma inhomogeneity (i.e., the direction of the plasma density and space potential profiles) further simplifies this process. However, care must be taken in this approach, especially in the vicinity of any very short scale gradients. This is a truly “local” calculation in that trends can be predicted at basically a single point instead of summing the contribution from the whole system from one boundary to the other.

The magnetic field is specified to lie along the  $z$ -axis, and the density and space potential profiles to be along the  $x$ -axis. The azimuthal direction will therefore be the  $y$ -axis (strictly,  $y = r\theta$ ). The linearized forms of Equations 4 to 6 are now utilized. First-order quantities will be denoted with a tilde (velocities are all first-order, except where specifically labeled).

### 1. Electron Perturbation

Collisional effects are ignored in the perpendicular direction for the same reasons that allowed their neglect in the equilibrium velocity equations. Next, let  $v_{e0} = \gamma_{e0} = v_{EB} - v_D$  represent the zero order expression for the electron velocity. The components of the momentum equation are then substituted in to the continuity equation to get

$$\eta_e = \chi \left[ \frac{-\omega_* \nu_{ce} + i k_z^2 v_{the}^2}{\hat{\omega} \nu_{ce} + i k_z^2 v_{the}^2} \right] \quad (19)$$

where

$$\hat{\omega} = \omega - \omega_{EB} = \omega - k_y \frac{\phi'_0}{B_0} \quad (20)$$

represents a doppler shift in the real part of the frequency ( $\omega_R$ ),

$$\omega_* = k_y \frac{KT_e}{eB_0} \frac{n'_0}{n_0} \quad (21)$$

is the diamagnetic drift frequency,

$$v_{the}^2 = \frac{KT_e}{m_e} \quad (22)$$

is the (squared) electron thermal speed, and the two new variables in the fluctuating quantities are given by

$$\eta_e \equiv \frac{\tilde{n}_e}{n_0} \quad \chi \equiv \frac{e\tilde{\phi}}{KT_e} \quad (23)$$

In fact, Equation 19 is a modified Boltzmann relation in the first order density and potential. This is well known in terms of the resistive drift instability [22–29]. Density perturbations will tend to travel azimuthally ( $y$ -direction) at the diamagnetic drift speed  $v_D$ . In the absence of electron collisions  $\eta = \chi$ , and the first order potential will oscillate in phase with the density perturbation creating a stable drift wave. Significant parallel electron collisions (they are magnetized azimuthally) will cause  $\eta \neq \chi$ . Density and potential perturbations will be de-phased such that a net outward ( $x$ -direction)  $\tilde{E} \times B_0$  electron flow will build up from the azimuthal electric fields due to charge separation creating an unstable situation. Inclusion of a non-zero space potential profile in Equation 19 simply doppler shifts the real part of the frequency and has no effect on the drift instability growth rate.

## 2. Ion Perturbation

In the first order expressions for the ion velocities the convective derivative term can no longer be neglected. Collisions will be separated into perpendicular ( $\nu_\perp$ ) and parallel ( $\nu_\parallel$ ) components to clarify their contribution in those directions. The zero order velocity is again  $v_{i0}\hat{y} = \gamma_{i0} = v_{EB}$ . Consider, first, the convective derivative part of the linearized momentum equation

$$(\vec{v} \cdot \nabla)\vec{v}_0 = \tilde{v}_x \gamma'_{i0} \hat{y} \quad (24)$$

$$(\vec{v}_0 \cdot \nabla)\vec{v} = \gamma_{i0} i k_y (\tilde{v}_x \hat{x} + \tilde{v}_y \hat{y} + \tilde{v}_z \hat{z}) \quad (25)$$

It is clear that the equilibrium ion velocity,  $\gamma_{i0}$ , now plays an important role in the first order description. The contribution from  $(\vec{v}_0 \cdot \nabla)\vec{v}$  gives the doppler shift to the real

part of the frequency, and the  $(\vec{v} \cdot \nabla)\vec{v}_0$  term gives rise to a shear effect. In particular, note that  $\gamma'_{i0} \sim \phi''_0$ . So, if the  $E_0 \times B_0$  azimuthal velocity is not constant along the radius ( $x$ -direction) due to a radial profile in  $\phi_0$ , the possibility of “slippage” in the rotation can occur from shearing ( $\phi''_0 \neq 0$ ) in the space potential profile. This creates a Kelvin-Helmholtz instability in the shear region where the energy in rotation of the two co-rotating fluids can be released [30–33]. However, the classic Kelvin-Helmholtz instability is brought about by energy exchange between the two fluids due to their viscosity, or collisions, between each species. This implies coulomb collisions in a plasma, whereas the present model only includes the effects of charge-neutral collisions. So, any Kelvin-Helmholtz mechanism in this model would be due to one species imparting a drag on the other species through electric field interaction from charge bunching at the layer. Even in the absence of an  $E_0 \times B_0$  velocity shear ( $\phi''_0 = 0, \phi'_0 \neq 0$ ), the Simon-Hoh instability [34,35] could still be an important factor if the density and space potential profiles are oppositely directed and  $\nu_e/\omega_c, \nu_i/\Omega_c \gg 1$ .

As before, the velocity components from the momentum equation are substituted in to the continuity equation. Furthermore, given the plasma parameters measured in this experiment, the frequency ordering relative to the detected fluctuations at  $\omega$  is

$$\omega, \omega_{EB}, \omega_* \ll \Omega_c \quad (26)$$

which permits dropping the  $\gamma''_{i0} \sim \phi'''_0$  terms. This gives

$$\begin{aligned} \frac{\hat{\omega}}{C_s^2 \chi} \eta_i = & -\frac{(k_x^2 + k_y^2)(\hat{\omega} + i\nu_\perp)}{\Omega_c(\Omega_c + \gamma'_{i0})} \\ & + \frac{ik_x \frac{n'_0}{n_0}(\hat{\omega} + i\nu_\perp)}{\Omega_c(\Omega_c + \gamma'_{i0})} - \frac{k_y \frac{n'_0}{n_0}}{\Omega_c + \gamma'_{i0}} + \frac{k_z^2}{(\hat{\omega} + i\nu_\parallel)} \\ & - \frac{i2k_x k_y \gamma'_{i0}(\hat{\omega} + i\nu_\perp)^2}{\Omega_c^2(\Omega_c + \gamma'_{i0})^2} + \frac{2k_y \gamma'_{i0}(\hat{\omega} + i\nu_\perp)}{\Omega_c(\Omega_c + \gamma'_{i0})^2} \end{aligned} \quad (27)$$

where the ion sound speed is defined as

$$C_s = \sqrt{\frac{KT_e}{M_i}} \quad (28)$$

### 3. Dispersion Relation

Equations 27 and 19 can now be combined using the plasma approximation relative to fluctuating quantities as well as in the equilibrium state  $\eta_e = \eta_i$  resulting in a quartic expression for the complex frequency  $\omega$ .

$$\begin{aligned} & \frac{\hat{\omega}}{C_s^2} \left[ \frac{-\omega_* \nu_{en} + i k_z^2 v_{the}^2}{\hat{\omega} \nu_{en} + i k_z^2 v_{the}^2} \right] + \frac{(k_x^2 + k_y^2)(\hat{\omega} + i \nu_{\perp})}{\Omega_c(\Omega_c + \gamma'_{i0})} \\ & - \frac{i k_x \frac{n'_0}{n_0}(\hat{\omega} + i \nu_{\perp})}{\Omega_c(\Omega_c + \gamma'_{i0})} + \frac{k_y \frac{n'_0}{n_0}}{\Omega_c + \gamma'_{i0}} - \frac{k_z^2}{(\hat{\omega} + i \nu_{\parallel})} \\ & + \frac{i 2 k_x k_y \gamma'_{i0}(\hat{\omega} + i \nu_{\perp})^2}{\Omega_c^2(\Omega_c + \gamma'_{i0})^2} - \frac{2 k_y^2 \gamma'_{i0}(\hat{\omega} + i \nu_{\perp})}{\Omega_c(\Omega_c + \gamma'_{i0})^2} = 0 \end{aligned} \quad (29)$$

This relation includes the effects of the resistive drift, Kelvin-Helmholtz, and Simon-Hoh mechanisms for low frequency instability in the framework of a linear two-fluid description. Two of the roots,  $\omega_4$  and  $\omega_3$ , are extremely high frequency and are properly treated only by using Poisson's equation. This and the frequency ordering (Equation 26) justifies their neglect as candidates. The two surviving roots are identified, without loss of generality, by invoking the local approximation ( $k_x \rightarrow 0$ ), neglecting collisions, and letting  $\phi'_0 \rightarrow 0$  giving the well known expression [37]

$$\omega_{1,2} = -\frac{\omega_*}{2} \pm \frac{1}{2} \sqrt{\omega_*^2 + 4 C_s^2 k_z^2} \quad (30)$$

where  $C_s^2 k_y^2 / \Omega_c^2 \ll 1$ . This is shown in Figure 3. These two roots are the accelerated and retarded ion acoustic wave branches [38], which can be seen by comparison with the acoustic wave slopes. Notice that the accelerated branch has a finite frequency for infinite wavelength ( $k_z \rightarrow 0$ ). This frequency is the diamagnetic drift frequency mentioned earlier ( $\omega_*$ ) and represents the zero  $k_z$  limit of the electrostatic drift wave. Only roots of Equation 30 lying on the accelerated ion acoustic wave branch will have positive imaginary parts  $\omega_I$  designating this branch as the focus of the instability investigation.

For generality, and in terms of the slab model presented here, shear can be thought of as a constant multiplier on  $\phi_0$  (which could be different at any point in space) representing a scale length over which the second derivative of  $\phi_0$  exists. The same applies for the first derivative of  $\phi_0$ . Thus, doppler shifting is represented by one variable multiplying  $\phi_0$ , and the addition of shear implies a second variable, to represent the shear magnitude, multiplying the first in the model.

Figure 4 gives the growth rate characteristic as a function of magnetic field for different ion masses. This shows that ion mass plays an important role in the growth rate *without* the inclusion of the magnetic viscosity tensor in the ion equations of motion. In other words, the instability shows a scaling with  $B_0$  without finite ion larmor radius effects included. Magnetic viscosity was not included in the analysis because the assumption  $T_i \rightarrow 0$  was made. In terms of the instability model, light ion gases will see a maximum instability growth rate at lower magnetic field strengths. The model also predicts low  $\omega_R$ .

### C. Perturbation Description in Cylindrical Geometry

To more accurately compare an individual root, or mode, to experiment, it is necessary to use a cylindrical geometry and assume a Fourier representation only in the directions of homogeneous plasma characteristics. The coefficients of the Fourier series representation of wave quantities will become functions of the spatial coordinates in the nonhomogeneous direction, turning the algebraic equations into a linear differential system.

#### 1. Dispersion Relation

Proceeding as before, the dispersion relation can be written as

$$\tilde{\phi}'' + B(r)\tilde{\phi}' + C(r)\tilde{\phi} = 0 \quad (31)$$

where

$$B(r) = -\frac{\frac{1}{r}\gamma'_{i0} - \frac{1}{r^2}\gamma_{i0}}{\gamma'_{i0} + \frac{1}{r}\gamma_{i0} + \Omega_c} - \frac{\frac{2}{r}\gamma'_{i0} - \frac{2}{r^2}\gamma_{i0}}{\frac{2}{r}\gamma_{i0} + \Omega_c} + \frac{1}{r} + \frac{n'_0}{n_0} \quad (32)$$

$$C(r) = \left[ -\frac{\hat{\omega}}{C_s^2} \left( \frac{-\omega_* \nu_{en} + i k_z^2 V_{th}^2}{\hat{\omega} \nu_{en} + i k_z^2 V_{th}^2} \right) + k_z^2 \right] \\ + \frac{\frac{m}{r} \left( \frac{1}{r}\gamma'_{i0} - \frac{1}{r^2}\gamma_{i0} \right) \left( \frac{2}{r}\gamma_{i0} + \Omega_c \right)}{(\hat{\omega} + i\nu_\perp) \left( \gamma'_{i0} + \frac{1}{r}\gamma_{i0} + \Omega_c \right)} \\ - \frac{\frac{m}{r} \frac{n'_0}{n_0} \left( \frac{2}{r}\gamma'_{i0} + \Omega_c \right)}{\hat{\omega} + i\nu_\perp} - \frac{m^2}{r^2} \quad (33)$$

and  $m$  is now the azimuthal mode number. Equation 31 is integrated from  $r = 0$  to the radial boundary,  $r = a$ , to find the eigenfunction,  $\tilde{\phi}(r)$ , subject to boundary conditions. These boundary conditions are based on experimental observation in this work and others [26] and are simply (valid for  $m \neq 0$ )

$$\tilde{\phi}(0) = \tilde{\phi}(a) = 0 \quad (34)$$

Figure 5 shows a comparison between the slab and cylindrical models in the absence of a space potential profile for an  $m = +1$  mode. The real and imaginary eigenfrequencies are calculated as a function of  $k_z$  and show good agreement. Addition of a non-zero space potential profile, however, points out the differences in the models. For the cylindrical model, a radial space potential profile of

$$\phi_0(r) = \Phi_0 \left[ \frac{(r/r_0)^c}{1 + (r/r_0)^c} \right] \quad (35)$$

is used to compare the calculated eigenfrequency with that of the slab model as a function of magnetic field strength, where  $c = 4$ ,  $r_0 = 4cm$ , and an  $m = +1$  mode is used. This is given in Figure 6. The difference in the two models is most apparent in  $f_R$ , whereas growth rates show better agreement.

The cylindrical model produces interesting results, in terms of the equilibrium space potential profile, if the condition

$$\omega_R - \omega_{EB} = \omega_R - \frac{m}{r} \frac{\phi'_0}{B_0} \rightarrow 0 \quad (36)$$

is met. In other words, when the real part of the eigenfrequency approaches, or is equal to, the  $E_0 \times B_0$  frequency at some radial location. As this condition is approached, the local index of refraction becomes singular. This is illustrated in Figure 7. As the region where Equation 36 is closest to being satisfied is approached, the radial wavelength of the eigenfunction decreases, and the eigenfunction magnitude decreases.

As  $k_r(r)$  approaches a singularity, the number of  $[\omega, k_z]$  pairs that satisfy Equation 31 transitions from discrete to continuous. This suggests the possibility of mode conversion at a local region. In order to treat this situation properly, however, the continuity equations for each species must be closed with Poisson's equation, and terms dropped due to the frequency ordering assumption of Equation 26 must be retained. Thus, in terms of the present cylindrical model, all that can be said is that the possibility of mode conversion can exist where  $\omega_R = \omega_{EB}$ .

Significant ion collisions can mitigate this effect as shown in Figure 8. Here, a space potential profile is chosen such that  $\omega_R$  is nearly equal to  $\omega_{EB}$  at two radial locations. Increasing the ion-neutral collision rate is shown to decrease the magnitude of  $k_r(r)$ .

In terms of the observed  $n_0(B_0)$  behavior and its correlation to large low frequency density fluctuations, the slab model gives a good representation of the instability behavior as a function of magnetic field, while the cylindrical model reveals the possibility of mode conversion.

### III. EXPERIMENT

#### A. Apparatus

The experimental apparatus is shown in Figure 9. The plasma chamber consists of the main and microwave sections. The microwave section allows excitation at  $2.45 \text{ GHz}$ , but was not used for the present experiment. Radial diagnostic access was achieved through

three sets of three 1/4-inch vacuum feed-through connections located 62.4, 96.4, and 130.3 *cm* downstream of flange 2. Axial diagnostic access was achieved through the back flange (3). Gas fill pressure was 8 *mTorr*.

Ten of the eleven coils, as noted in Figure 9, were used to create a coaxial static magnetic field of up to 1500 Gauss. The field varied by less than 8 percent over the length shown. Radiofrequency (rf) power was fed, via a capacitive matching network, to an R-antenna [40] at 13.56 *MHz*. Input power was 2 - 2.2 *kW* and matched to keep reflections  $\leq 10$  %. The experiment was operated in a pulsed mode with an extremely low duty cycle. Magnetic field strength was allowed to “flatten” (due to the coils’ inductance) before the rf power was turned on. Duration time of the rf was 100 *mS* with diagnostic triggering at 40 *msec* after rf power was switched on.

The antenna length was 24 *cm* and located with its midplane 33 *cm* downstream of flange 2. The magnetic field pointed from flange 2 to 3, designating the  $\hat{z}$  direction.

## B. Diagnostics

Equilibrium plasma parameters ( $n_0$ ,  $V_s$ ,  $V_f$ , and  $T_e$ ) were measured using rf compensated Langmuir probes [41].

Ion flow velocities parallel to  $B_0$  were measured using mach probes [42–45,19,46]. Care was taken to ensure that their disturbance length was much less than any axial equilibrium gradient. Parallel ion velocities were calculated from the relation

$$M = \frac{v}{C_s} = \sqrt{\frac{v^2 M_i}{K T_e}} \quad (37)$$

where  $M$  and  $v$  denote the mach number and parallel velocity respectively. Note that  $T_i \rightarrow 0$  in this experiment and therefore  $T_i$  does not contribute to  $C_s$ , facilitating the calculation of actual ion flow velocities.

The time averaged cross-field particle flux, for a particular species, due to fluctuations in potential and density is given as

$$\Gamma_{\perp} = \langle \tilde{n} \tilde{v}_{\perp} \rangle = \left\langle \tilde{n} \frac{\tilde{E}_{\theta} \times B_0}{|B_0|^2} \right\rangle = \left\langle \frac{\tilde{n} \tilde{E}_{\theta}}{B_0} \right\rangle \quad (38)$$

where electrostatic fluctuations will be assumed

$$\tilde{E}_{\theta} = -ik_{\theta} \tilde{\phi} \quad (39)$$

Taking the Fourier transform of fluctuating quantities, the radial flux can be written as [47–49]

$$\Gamma_{\perp} = \frac{2}{B_0} \int_0^{\infty} k_{\theta} |\gamma_{n\phi}(\omega)| \sin[\alpha_{n\phi}(\omega)] \tilde{n}_{rms} \tilde{\phi}_{rms} d\omega \quad (40)$$

where  $\alpha_{n\phi}$  is the phase angle between density and potential fluctuations and the coherence spectrum is defined as

$$|\gamma_{n\phi}(\omega)| = \frac{|P_{n\phi}(\omega)|}{\sqrt{P_{nn}(\omega)P_{\phi\phi}(\omega)}} \quad (41)$$

$P_{ii}$  and  $P_{ij}$  are the auto- and cross- spectra respectively. The coherence spectrum can be interpreted as the degree of cross correlation between the two signals.

Radial flux was measured using a triple probe technique. The probe is shown in Figure 10. Measurement of  $\alpha_{n\phi}$ ,  $\tilde{n}_{rms}$ , and  $\tilde{\phi}_{rms}$  was implemented using the  $\tilde{n}$  and  $\tilde{\phi}_f$  tips lying on the same  $B_0$  line.

The wavenumber  $k_{\theta}$  was measured using the two  $\tilde{\phi}_f$  tips, which were separated azimuthally by a small distance  $\Delta x$ . The phase difference  $\psi_{12}$  of the cross spectral density measurement between them gives

$$k_{\theta}(\omega) = \frac{\psi_{12}}{\Delta x} \quad (42)$$

The upper limit of  $k_{\theta}$  is set by  $\Delta x$  and the point at which branching of the inverse tangent function in calculating  $\psi_{12}$  is reached; while the lower limit is set by the accuracy of the  $\psi_{12}$  measurement. Each data point in the fluctuating quantities was averaged over several shots. This gave the upper and lower bounds on the wavenumber as

$$0.13 < |k_{\theta}| < 7.6 \quad cm^{-1} \quad (43)$$

Density fluctuations were measured by biasing an uncompensated probe tip in the ion saturation region. The bias was kept negative enough to avoid rf effects on the ion saturation current [41]. The measurement resistor and cable length for the tip gave no significant low pass filtering effects on the signal in magnitude or phase below 10 *MHz* - which is three orders of magnitude above the detected frequency of fluctuations. Displacement current due to the sheath capacitance was also found to be insignificant.

Ideally, fluctuations in the space potential would be measured. This, however, proves to be extremely difficult in terms of electrostatic probe methods. It is much easier to measure fluctuations in the floating potential. The relation between space and floating potentials in a Maxwellian plasma is

$$\phi_s - \phi_f = \frac{KT_e}{e} \left( 3.33 + \frac{1}{2} \ln \mu \right) \quad (44)$$

where  $\mu$  is the ion mass relative to hydrogen. As long as  $T_e$  does not change on the equilibrium timescale  $\phi_s - \phi_f$  remains constant, and the fluctuations in floating potential are identical in magnitude and phase to those of the space potential.  $T_e$  was observed to be constant on the equilibrium timescale of this experiment by implementing fast probe traces at different times during the rf input.

Correct measurement of floating potential fluctuations  $\tilde{\phi}_f$  dictates that the probe tip draw no plasma current during all phases of the rf cycle. Sheath capacitance at the probe tip, as mentioned earlier, can be neglected. In order to negate capacitive effects in the coaxial measurement system, a capacitance neutralization technique was used as shown in Figure 11. Here, the probe tip is at an extremely high impedance dictated by the operational amplifier. Driving the middle and center conductors at the same voltage alleviates any capacitance along the length of the probe. The low amplifier output impedance drives any small capacitance  $C_{2stray}$  as well.

## IV. RESULTS

### A. Measurement Accuracy and Error

The probe placement error is estimated to be  $\pm 2mm$  over 6 *cm*, or about 3 percent.

Langmuir probe current-voltage (CV) traces were averaged over several shots. Plasma parameters calculated from probe CV traces taken at different times for the same input conditions showed an error of less than ten percent.

Regarding measurement of fluctuating quantities, forty individual waveforms were stored digitally for each data point. Standard deviations were ten to fifteen percent.

Individual mach probe waveforms were stored digitally. However, a computer program tracked the real-time standard deviation; and it was kept to less than one percent.

Unless otherwise mentioned, presented data corresponds to measurements taken 33 *cm* downstream of the antenna midplane in helium at 8 *mTorr* fill pressure. Rf input power was kept at 2 *kW* at 13.56 *MHz*.

### B. Equilibrium Plasma Parameters

Radial measurements of the equilibrium plasma parameters  $n_0$ ,  $T_e$ ,  $\phi_0$ , and  $\phi_f$  are given in Figures 12 to 14. As the magnetic field is increased,  $n_0(r)$  becomes more peaked while  $T_e$ ,  $\phi_0$ , and  $\phi_f$  are high at the lowest  $B_0$ , decrease, and then increase slightly. Radial profiles of  $T_e$  show high electron temperatures at the plasma edge. Space potential profiles show off-axis maxima above 300 *G*, while floating potential profiles remain relatively flat.

### C. Fluctuation Measurements

Figures 15 to 18 give spectrograms of ion saturation biased probe signals and their corresponding equilibrium plasma density as a function of magnetic field strength for the gases used in this work. Note that the light ion gases, hydrogen and helium, show a peaking

in  $n_0(B_0)$  whereas heavier ion gases, neon and argon, show a saturation in  $n_0(B_0)$ . This has also been reported by Sakawa *et al.* [10]. Detected fluctuation frequencies at higher  $B_0$  are  $\leq 2$  kHz. Figure 19 gives the dominant low frequency fluctuating quantities behavior as a function of  $B_0$  in helium. This shows a critical  $B_0$  at which  $\tilde{n}$  and  $\tilde{\phi}$  begin to acquire significant magnitudes.

Figures 20 and 21 give radial profiles of both equilibrium and fluctuating parameters at different magnetic field strengths. For all cases, normalized  $\tilde{n}(r)$  and  $\tilde{\phi}(r)$  have off-axis maxima.

#### D. Parallel Ion Flow Measurements

In these measurements, a positive mach number corresponds to a flow in the  $-z$  direction - toward flange number 1. All measurements were performed in helium. Figure 22 gives radial mach number profiles at different  $B_0$ . In all cases, the ion flow is very small compared to the sound speed and reverses direction (from  $+z$  to  $-z$ ), near the axis, above 1 kG.

Figure 23 shows axial mach number profiles at different  $B_0$ . Note the significant increase of parallel ion flow under the antenna, toward flange 1, above 850 G.

#### E. Radial Flux

These measurements were performed in helium as well. Figure 24 shows the radial flux measured at  $r = 2$  cm versus  $B_0$ . An extremely large perpendicular flux is evident between 600 and 1200 Gauss.

### V. DISCUSSION

The theoretical model included the effects of charge-neutral collisions and equilibrium space potential profile on the accelerated ion acoustic wave dispersion relation assuming cold ions (finite ion larmor radius effects were neglected). Thus, ion mass plays a role in

the growth rate without the addition of the magnetic viscosity tensor in the ion equations of motion. For example, when the ion larmor radius is comparable to the perpendicular wavenumber ( $k_{\perp}\rho \approx 1$ ) it has been shown that damping of the mode will occur [20,24]. Furthermore, the effects brought about when  $\omega_R = \omega_{EB}$  can greatly affect the mode behavior.

Based on measurements,  $\tilde{\phi}/T_e$  envelope data correspond to azimuthal mode numbers of 1 to 10, validating a modal picture of the wave behavior as given in the theory. Furthermore, as the theory has shown, the parallel wavenumber is most likely small; since for large  $k_z$ , the mode is stable, and collisions or even shear do not de-stabilize the mode. Furthermore,  $\omega_R$  is very high at large  $k_z$ , and the measured frequency is low ( $\leq 1 - 2$  kHz).

### A. Mode Identification

In what follows, the behavior of the observed mode will be interpreted in terms of the resistive drift and Kelvin-Helmholtz instabilities, with a general discussion of the effects of the singularity in  $k_r(r)$ . Since  $\nu_{en}/\omega_c, \nu_{in}/\Omega_c \ll 1$  in this experiment, the Simon-Hoh mechanism plays an insignificant role.

#### Resistive drift mode

The experimentally observable characteristics of this mode are given as [24]

- driven by density gradient.
- $\tilde{n}/n_0$  amplitude is maximum at maximum in radial density gradient.
- the phase velocity of the wave goes as  $v_{De}$  - the electron diamagnetic drift velocity.
- amplitudes of  $\tilde{n}/n_0$  and  $\tilde{\phi}/T_e$  are approximately equal.
- $\alpha_{n\phi}$  remains relatively constant with radius unless the collision rate changes along the radius.

#### Kelvin-Helmholtz instability

The observable characteristics of the Kelvin-Helmholtz instability [32] are

- driven by azimuthal velocity shear (shear in  $v_{EB}$ ).
- $\tilde{n}/n_0, \tilde{\phi}/T_e$  amplitudes are maximum in velocity shear region.
- $\alpha_{n\phi}$  varies as shear layer is crossed.
- Amplitude of  $\tilde{n}/n_0 < \tilde{\phi}/T_e$ .
- $\omega_R \approx (0.2 - 0.5) \times v_{EB}(max)/r$ .

Referring to Figure 20, the characteristics outlined above for the drift wave can be verified in the measured parameters at  $B_0 = 300G$ . Note first that the magnitudes of  $\tilde{n}/n_0$  and  $\tilde{\phi}/T_e$  are relatively equal, and that the maximum in  $\tilde{n}/n_0$  does seem to correspond to the maximum in density gradient. The  $\tilde{\phi}/T_e$  profile shows a second maximum close to  $r = 0$ , but this is at a point where  $\tilde{n}/n_0$  is minimum. At the location of high potential and density fluctuations, the measured perpendicular wavenumber  $k_\theta$  follows a monotonic profile corresponding to  $m \approx 3$ . The angle between  $\tilde{n}$  and  $\tilde{\phi}$  is not constant in this region, however, but does show a monotonic behavior. An azimuthal mode number of 3, combined with the measured density profile and temperature, gives a drift frequency of  $13.3KHz$  compared to a measured frequency of  $\approx 11KHz$ . The rotation direction is  $+\theta$ , which corresponds to the electron diamagnetic drift direction. The space potential profile varies only slightly over the radius. Interestingly enough, the magnitude of  $\tilde{n}/n_0$  also appears where a slight “kink” in the space potential profile exists. However, the relatively equal magnitudes of  $\tilde{n}/n_0$  and  $\tilde{\phi}/T_e$  and the measured frequency point toward a resistive drift wave mode.

In Figure 21, the radial space potential profile changes from relatively flat to a region where it increases about  $25V$  over  $4cm$  starting at  $r = 2cm$ . Profiles of  $\tilde{n}/n_0$  and  $\tilde{\phi}/T_e$  both reach maxima at that location as well. The magnitude of  $\tilde{\phi}/T_e$  is about 5 times greater than  $\tilde{n}/n_0$ . The angle between  $\tilde{n}$  and  $\tilde{\phi}$  changes rapidly in this region and  $k_\theta$  goes from rapidly changing to  $+\hat{\theta}$  rotation with  $m \approx 1 - 3$ . The rotation corresponds to the  $E \times B$  direction from  $r = 2 - 6cm$  (which is also the electron drift velocity direction). However, the frequency characteristic in the region from 2 to  $6cm$  is

$$f_{EB} \approx \frac{1}{2\pi} \frac{(1-3)}{r} \frac{25/0.04}{0.06}$$

or roughly  $50 - 150 KHz$ . This is a factor of  $10 - 50$  greater than the measured frequency of  $2 - 3.5 KHz$ . The drift frequency in this case is  $\approx 20 KHz$ . Aside from the frequency discrepancy, it appears that the Kelvin-Helmholtz mechanism dominates here.

Similar arguments can be made for all of the radial fluctuation profile data taken, with the result that the observed instability does not lend itself completely to either mechanism.

### B. $k_r$ Singularity

The possible effects of the singularity in  $k_r(r)$  when  $\omega_R = \omega_{EB}$  were discussed earlier. These included local mode conversion, which must always go to a shorter wavelength mode. However, short wavelengths are relatively stable in terms of the theoretical model presented here. Reference to Figure 25 shows that in the general region of magnetic field strength corresponding to enhanced radial transport, it does not appear to play a role. In magnetic field regions of negligible radial transport, the possibility of the singularity becoming important exists at a radial location where significant gradients also exist.

### C. Growth Rate and Losses

The growth rate calculated from the slab model for helium and its correlation with  $\tilde{n}$  and  $\tilde{\phi}$  are shown in Figure 19 as a function of  $B_0$ . Note how the maximum growth rate corresponds strongly with the maximum in  $\tilde{\phi}$  and the point where  $\tilde{n}$  drastically jumps.

Figures 16 and 15 show the growth rate calculated from the slab model along with the corresponding spectrogram of  $\tilde{n}$  fluctuations and  $n_0$  versus  $B_0$  profiles for helium and hydrogen respectively. Note the strong correlation between the onset of low frequency fluctuations, maximum in growth rate, and fall-off in density.

Parallel and perpendicular escape times were calculated from the measurements of parallel flow and perpendicular flux and presented in Figure 26. This shows that between 700

and 1100 Gauss, the perpendicular escape time is between 10 and 100 times *smaller* than the parallel escape time. This correlates with

- the theoretical maximum predicted growth rate in helium from the slab model (Figure 16)
- the point at which the measured  $\tilde{n}/n_0$  begins a dramatic rise (Figure 19(a))
- the location of maximum  $\tilde{\phi}/\phi_0$  (Figure 19(b))
- the flattening in the  $n_0$  versus  $B_0$  profile (Figure 16)

This result alone, however, does not fully explain the observed  $n_0$  decrease at the highest magnetic fields. Note that the density steadily decreases with increasing  $B_0$  above 1KG, whereas  $\tau_{\perp}$  and  $\tau_{||}$  are larger than  $\tau_{||}$  measured under the antenna. It is possible for the ions to gain increased energy from large electric fields in the antenna near field. The distance which an ion must travel to escape is decreased because the antenna is closer to one end of the plasma chamber. This shows that the ions could be escaping more effectively in the axial direction at higher magnetic fields. Thus, at high magnetic field strengths, Figure 26 reveals that both radial and axial loss rates can contribute to the overall loss. These results describe the observed density versus magnetic field strength characteristic in this experiment.

## VI. CONCLUSIONS

The observed behavior of the plasma density as a function of magnetic field is now understood in terms of an instability. Up to a critical magnetic field strength the plasma density increases monotonically. High frequency instabilities resembling the resistive drift mode are present, but do not affect losses significantly. The increase in plasma density with  $B_0$  in this region corresponds to antenna coupling and wave energy deposition. As the critical magnetic field value is reached, an azimuthally rotating low frequency electrostatic instability grows and eventually gives rise to enhanced radial transport with a magnitude

sufficient to significantly degrade plasma confinement. As  $B_0$  is increased even further, the instability is still present, but the radial transport is much lower in magnitude. In this region, enhanced axial loss dominates the radial loss as ions created at the antenna with sufficient axial velocities to again significantly degrade the plasma confinement.

Identification of the observed instability is not straightforward; it exhibits characteristics of both resistive drift and Kelvin-Helmholtz instabilities and is most likely a complex combination of the two. The instability arises from the accelerated ion acoustic wave branch, as determined from the dispersion relation. Measured frequencies were somewhat lower than that predicted by the slab theory, and the role of the singularity in  $k_r(r)$  when  $\omega_R = \omega_{EB}$  is not yet completely understood. Theoretical growth rates predicted for different ion mass show excellent correlation with observed equilibrium density decrease and measured fluctuation amplitude maxima as a function of magnetic field strength, and onset of maximum fluctuation amplitude for low frequencies in spectrograms of  $\tilde{n}$  versus  $B_0$ .

## VII. FIGURE CAPTIONS

Figure 1. Equilibrium plasma density versus magnetic field strength in a helicon source.

R-antenna, 8 *mTorr* fill pressure, 2 *kW* input power.

Figure 2. Signal from a 5 turn  $\partial B/\partial t$  probe connected via a center tapped 1 : 1 transformer to an analog storage oscilloscope. The signal frequency is 13.56 *MHz*. Vertical and horizontal scales are 20 *mV* and 1 *mS* per division respectively.

Figure 3. Two branches of Equation 30 in the limit of zero collisions and  $\phi_0, \phi'_0 \rightarrow 0$ .

Figure 4. (a) frequency and (b) growth rate,  $\gamma_I = \omega_I/2\pi$ , versus  $B_0$  with ion mass as a parameter.  $k_x = k_y = 30/m$ ,  $k_z = 0.15/m$ ,  $\nu_{en} = 10^7$ ,  $\nu_{\perp} = \nu_{\parallel} = 10^3$ , first derivative multiplier on  $\phi_0$  (*ef1*) = 150, second derivative multiplier on  $\phi_0$  (*ef2*) = 100,  $T_e = 5$  eV. The plasma density profile is represented as  $n'_0/n_0 = 1/a$  where  $a$  is the radial boundary (6 *cm*).

Figure 5. (a) frequency and (b) growth rate behavior of the accelerated ion acoustic wave branch for cylindrical (points) and slab (lines) models in the absence of an equilibrium space potential profile.  $B_0 = 1kG$ ,  $\nu_{en} = 10^8$ ,  $\nu_{\perp, \parallel} = 0$ . For the slab model,  $k_x = 60/cm$ ,  $k_y = 30/cm$ . The density profile in the cylindrical model is parabolic:  $n(r)/n_0 = (1 - r/a)^2$ .

Figure 6. (a) frequency and (b) growth rate versus  $B_0$  for both models (cylindrical - points, slab - lines).  $k_z = 0.5/m$ ,  $\nu_{en} = 10^8$ ,  $\nu_{\perp, \parallel} = 10^3$ . In the cylindrical model,  $\Phi_0 = 5$  and the density profile is identical to that of Figure 5. For the slab model,  $k_x = 52$ ,  $k_y = 16.7$ , *ef1* = 5, and *ef2* = 25.

Figure 7. Radial wavelength bunching as the singularity in  $k_r(r)$  is approached. (a)  $\omega_R - \omega_{EB}$ , (b)  $Re[\tilde{\phi}(r)]$ , and (c)  $Im[\tilde{\phi}(r)]$ .  $\omega = 2\pi(479.4 - i 154.3)$ ,  $B_0 = 1kG$ ,  $\nu_{en} = 10^8$ ,  $\nu_{\perp, \parallel} = 10^3$ . Density profile is identical to that of Figure 5.

Figure 8. Effect of ion collisions on the singular nature of  $|k_r(r)|$ . (a)  $k_r(r)$  for  $k_z = 0.25/m$ ,  $\nu_{en} = 10^7$ ,  $\omega = 2\pi(7725 + i 674)$ . (b) the left singular point with  $\nu_{\perp,\parallel}$  as a parameter.

Figure 9. Experimental apparatus. The total plasma chamber is 15.2 *cm* in diameter and 1.65 *m* in length. The main section is Pyrex while the microwave section is nonmagnetic stainless steel; and they are connected via mating flange number 2. Gas is fed into the chamber through a 1/4-inch diameter port located on flange number 1.

Figure 10. Probe used to measure the fluctuation induced radial flux.

Figure 11. Triaxial probe with capacitance neutralization circuit.

Figure 12. Radial density profiles at different  $B_0$ . The vertical scale for each graph is  $10^{13}/cm^3$ .

Figure 13. Radial electron temperature profiles with  $B_0$  as a parameter. The vertical scale for each graph is *eV*.

Figure 14. Radial space and floating potential profiles as  $B_0$  is varied. Space potential profiles are filled circles and floating potential profiles are open circles. The vertical scale for each graph is *V*.

Figure 15. Spectrogram of  $\tilde{n}$  fluctuations in *dBm* versus  $B_0$  in hydrogen. A Langmuir probe was placed at radial access port number one and biased to  $-100$  *V* at  $r = 2.5$  *cm*. The density profile (points connected by a line), and theoretical instability growth rate,  $\gamma_I$ , (line) versus  $B_0$  are given below.  $H = -14$  *dBm* and  $L = -23.5$  *dBm*.

Figure 16. Same as Figure 15 but for helium.  $H = -7.1$  *dBm* and  $L = -24.1$  *dBm*.

Figure 17. Same as Figure 15 but for neon.  $H = -10.1$  *dBm* and  $L = -24.5$  *dBm*.

Figure 18. Same as Figure 15 but for argon.  $H = -9.9$  *dBm* and  $L = -26.1$  *dBm*.

Figure 19. Fluctuation characteristics as a function of  $B_0$  in helium. (a)  $\tilde{n}/n_0$ . (b)  $\tilde{\phi}/T_e$ . (c)  $\alpha_{n\phi}$ . (d) Measured fundamental frequency (line) and measured  $k_\theta$  (points connected by a line).

Figure 20. Radial profiles of fluctuating quantities at 300 G. (a)  $\tilde{n}/n_0$  (points connected by a line) and  $n_0$  (line). (b)  $\tilde{\phi}/T_e$  (line),  $\phi_0$  (points), and smooth fit to  $\phi_0$  (dashed line). (c)  $\alpha_{n\phi}$ . (d) Measured fundamental frequency (points) and measured  $k_\theta$  (line).

Figure 21. Radial profiles of fluctuating quantities at 600 G. (a)  $\tilde{n}/n_0$  (points connected by a line) and  $n_0$  (line). (b)  $\tilde{\phi}/T_e$  (line),  $\phi_0$  (points), and smooth fit to  $\phi_0$  (dashed line). (c)  $\alpha_{n\phi}$ . (d) Measured fundamental frequency (points) and measured  $k_\theta$  (line).

Figure 22. Mach number radial profiles at different  $B_0$ . Measurements were taken at radial access port number 1.

Figure 23. Mach number axial profiles at different  $B_0$ . Measurements were taken at  $r = 0$ . Shaded regions correspond to the antenna location.

Figure 24. Measured radial flux versus magnetic field strength. Measurement taken at radial access port number 1 at  $r = 2$  cm.

Figure 25. Comparison of calculated  $f_{EB}$  radial profile with the measured fundamental frequency radial profile.  $f_{EB}$  was calculated from a third order polynomial fit to the measured space potential profile and assuming an appropriate  $m$  number from the data (1 or 3).

Figure 26. Parallel and perpendicular confinement times.  $\tau_{||}$  at radial access port number 1 (dashed line),  $\tau_{\perp}$  at the same location (line), and  $\tau_{||}$  under the antenna (points connected by a line).

## REFERENCES

- [1] R. W. Boswell, Phys. Lett., **33A**, 457 (1970); Plasma Phys. and Controlled Fusion, **26**, 1147 (1984).
- [2] F. F. Chen, Plasma Phys. and Controlled Fusion, **3**, 339 (1991).
- [3] M. A. Liebermann and A. J. Lichtenberg, *Principles of Plasma Discharges and Materials Processing* (Wiley, New York, 1994).
- [4] M. A. Liebermann and R. A. Gottscho in G. Hass, editor, *Physics of Thin Films* (Academic, New York, 1994).
- [5] E. E. Scime, P. A. Keiter, M. W. Zintl, M. M. Balkey, J. L. Kline, and M. Koepke, Plasma Sources Sci. Technol., **7**, 186 (1998).
- [6] F. R. Chang Diaz, J. P. Squire, R. D. Bengston, B. N. Breizmann, F. W. Baity, and M. D. Carter, Proceedings of the 36th AIAA/ASME/ASEE Joint Propulsion Conference, (American Institute of Aeronautics and Astronautics, Reston, VA, 2000), No. 2000-3756.
- [7] R. W. Boswell and F. F. Chen, I.E.E.E. Trans. on Plasma Sci., **25**, 1229 (1997).
- [8] F. F. Chen and D. Arnush, Phys. Plasmas, **4**, 3411 (1997).
- [9] F. F. Chen and D. D. Blackwell, Phys. Rev. Lett., **82**, 2677 (2000).
- [10] Y. Sakawa, T. Takino, and T. Shoji, Phys. Plasmas, **6**, 4759 (1999).
- [11] A.J. Perry and R.W. Boswell, J. Vac. Sci. Technol. B, **9**, 310 (1991).
- [12] J.H. Kim and H.Y. Chang, Phys. Plasmas, **3**, 1462 (1996).
- [13] P.A. Keiter, E.E. Scime, and M.M. Balkey, Phys. Plasmas, **4**, 2741 (1997).
- [14] D.A. Schneider, D.D. Borg, and I.V. Kamenski, Phys. Plasmas, **6**, 703 (1999).
- [15] F.F. Chen, J. Vac. Sci. Technol. A, **10**, 1389 (1992).

- [16] F.F. Chen, *Introduction to Plasma Physics and Controlled Fusion* (Plenum, New York, 1984).
- [17] D. Bohm, E.H.S. Burhop, and H.S.W. Massey, In A. Guthrie and R.K. Wakerling, editors, *The Characteristics of Electrical Discharges in Magnetic Fields* (McGraw-Hill, New York, 1949).
- [18] L. Spitzer, *Phys. Fluids*, **3**, 659 (1960).
- [19] P. C. Stangeby and G. M. McCracken, *Nucl. Fusion*, **7**, 1225 (1990).
- [20] Francis F. Chen, *Phys. Fluids*, **5**, 912 (1965).
- [21] S. J. Levinson, J. M. Beall, E. J. Powers, and R. D. Bengston, *Nucl. Fusion*, **5**, 527 (1984).
- [22] Francis F. Chen, *Phys. Fluids*, **4**, 1448 (1961).
- [23] Francis F. Chen, *Phys. Fluids*, **10**, 1647 (1967).
- [24] H. W. Hendel, T. K. Chu, and P. A. Politzer, *Phys. Fluids*, **11**, 2426 (1968).
- [25] T. K. Chu, B. Coppi, H. W. Hendel, and F. W. Perkins, *Phys. Fluids*, **12**, 203 (1969).
- [26] R. F. Ellis, E. Marden-Marshall, and R. Majeski, *Plasma Phys.*, **22**, 113 (1980).
- [27] N. D'Angelo and R. W. Motley, *Phys. Fluids*, **6**, 422 (1963).
- [28] Herbert Lashinsky, *Phys. Rev. Lett.*, **12**, 121 (1964).
- [29] L. G. Schlitt and H. W. Hendel, *Phys. Fluids*, **15**, 1578 (1972).
- [30] Gerald I. Kent, Norman C. Jen, and Francis F. Chen, *Phys. Fluids*, **12**, 2140 (1969).
- [31] D. L. Jasby, *Phys. Rev. Lett.*, **25**, 1567 (1970).
- [32] D. L. Jasby, *Phys. Fluids*, **15**, 1590 (1972).
- [33] F. W. Perkins and D. L. Jasby, *Phys. Fluids*, **14**, 102 (1971).

- [34] F. C. Hoh, Phys. Fluids, **6**, 1184 (1963).
- [35] Albert Simon, Phys. Fluids, **6**, 382 (1963).
- [36] David. D. Blackwell, Private Communication (1996).
- [37] B. B. Kadomtsev, *Plasma Turbulence*, (Academic, New York, 1965).
- [38] Nicholas A. Krall and Alvin W. Trivelpiece, *Principles of Plasma Physics*, (San Francisco, San Francisco, 1986).
- [39] David L. Book, Naval Research Laboratory Plasma Formulary, 1987.
- [40] Max Light and Francis F. Chen, Phys. Plasmas, **4**, 1084 (1995).
- [41] Isaac D. Sudit and Francis F. Chen, Plasma Sources Sci. Technol., **3**, 162 (1994).
- [42] P. C. Stangeby, Nucl. Fusion, **22**, 1383 (1982).
- [43] I. H. Hutchinson, Phys. Rev. A, **37**, 4358 (1988).
- [44] G. F. Matthews, Plasma Phys. Control. Fusion, **36**, 1595 (1994).
- [45] K. S. Chung and I. H. Hutchinson, Phys. Rev. A, **38**, 4721 (1988).
- [46] B. LaBombard, R. W. Conn, Y. Hirooka, R. Lehmer, W. K. Leung, R. E. Nygren, Y. Ra, G. Tynan, and K. S. Chung, J. Nuc. Materials, **162**, 314 (1989).
- [47] E. J. Powers, Nucl. Fusion, **14**, 749 (1974).
- [48] J. M. Beall, Y. C. Kim, and E. J. Powers, J, Appl. Phys., **53**, 3933 (1982).
- [49] S. J. Levinson, J. M. Beall, E. J. Powers, and R. Bengston, Nucl. Fusion, **24**, 527 (1984).

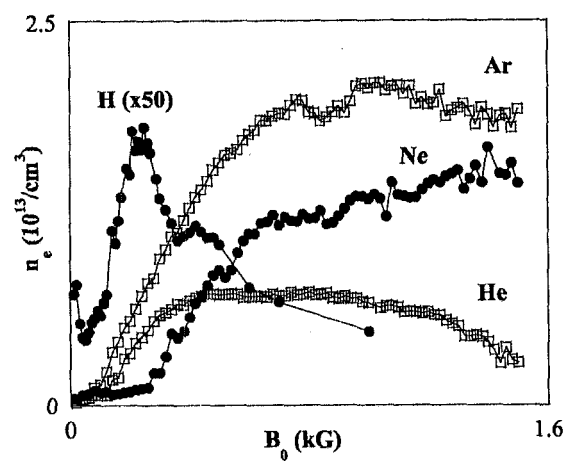


Fig. 1

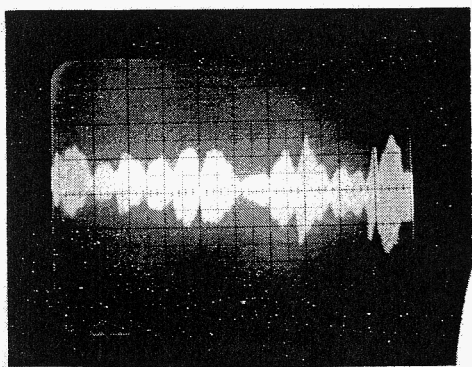


Fig. 2

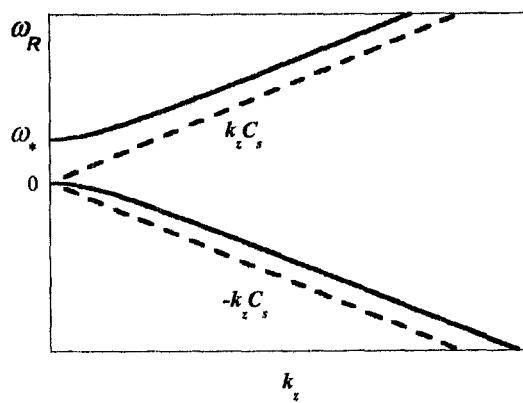


Fig. 3

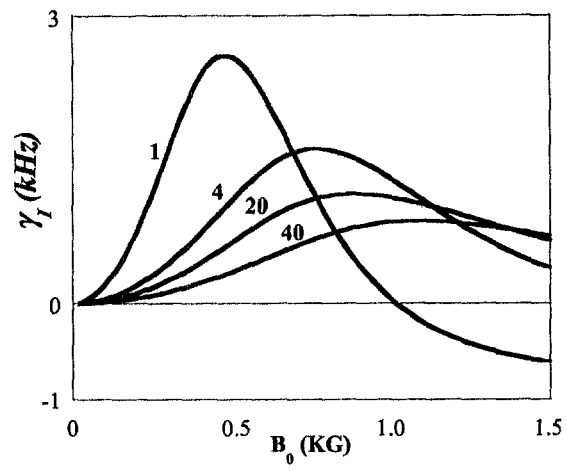


Fig. 4

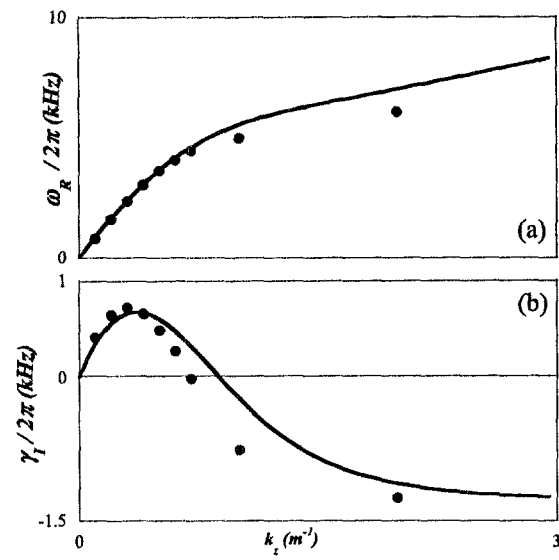


Fig. 5

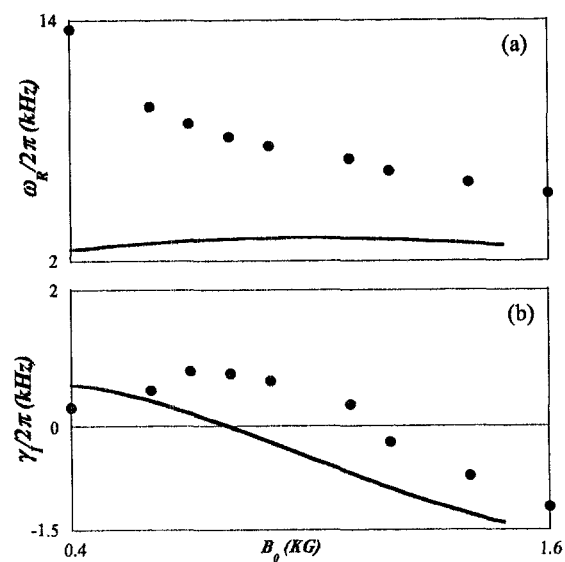


Fig. 6

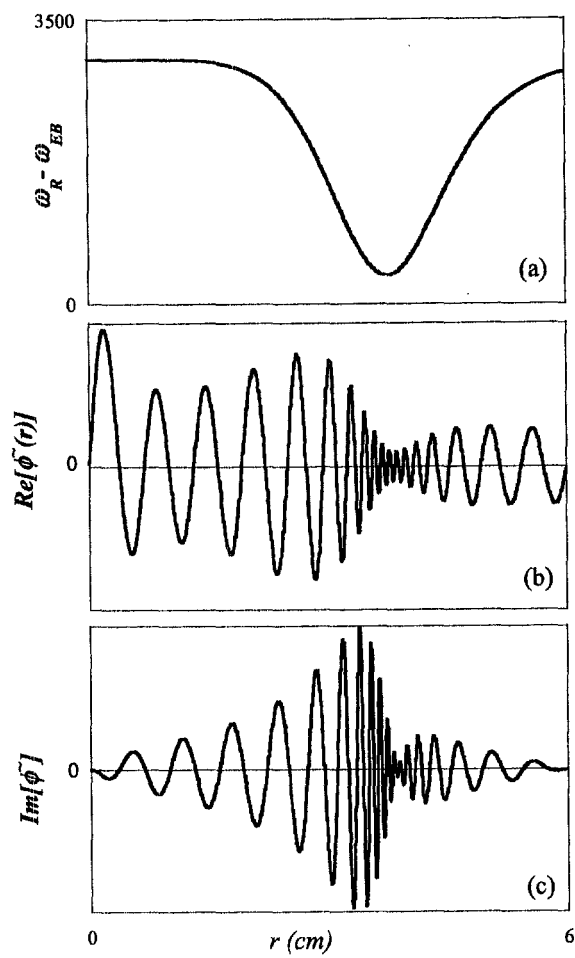


Fig. 7

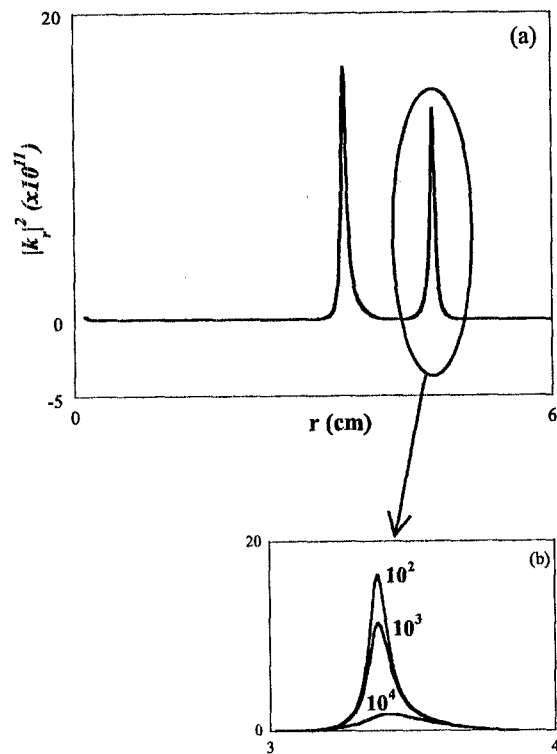


Fig. 8

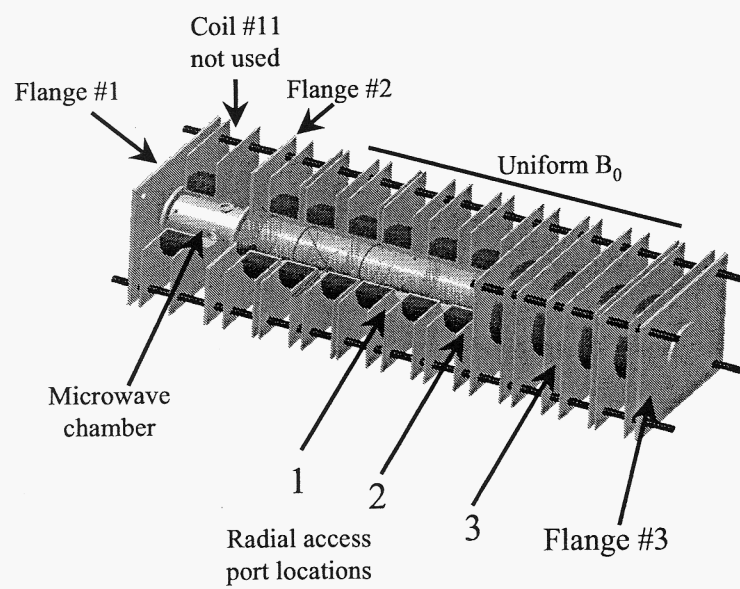


Fig. 9

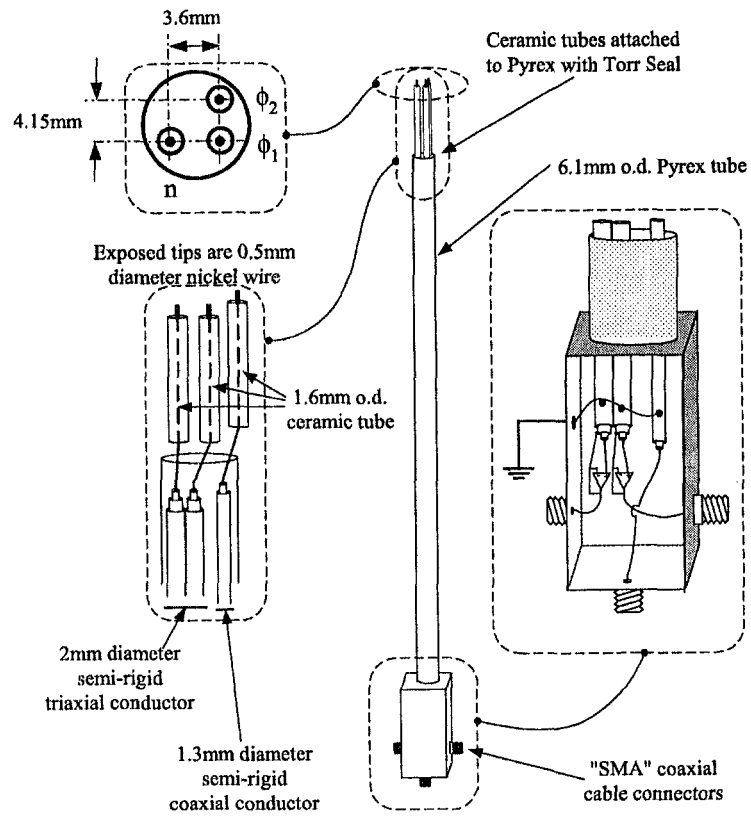


Fig. 10

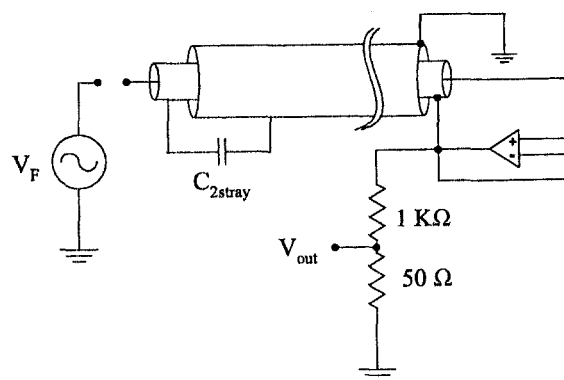


Fig. 11

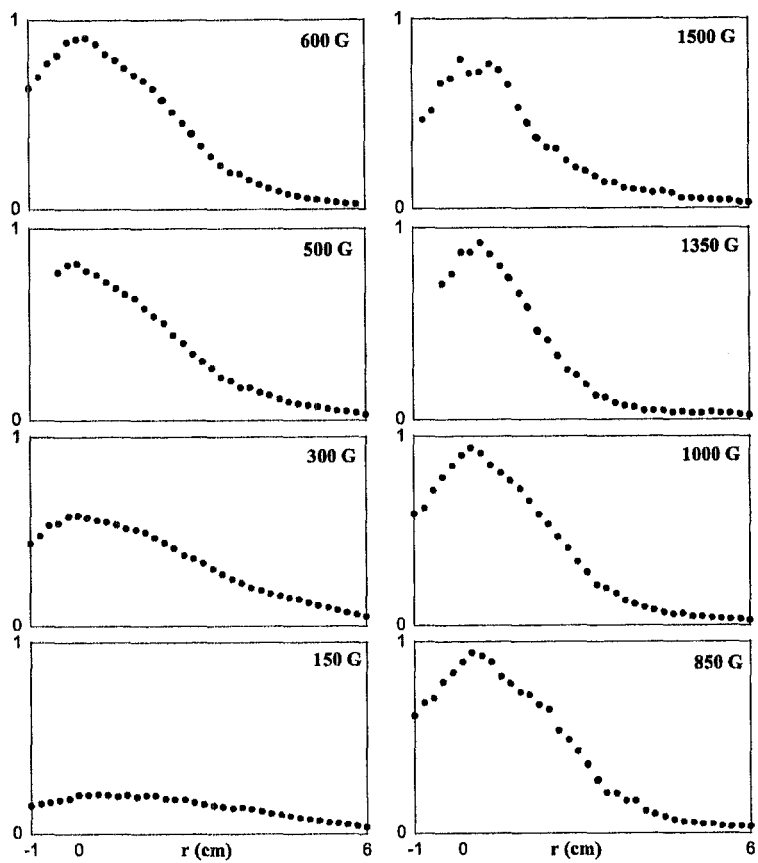


Fig. 12

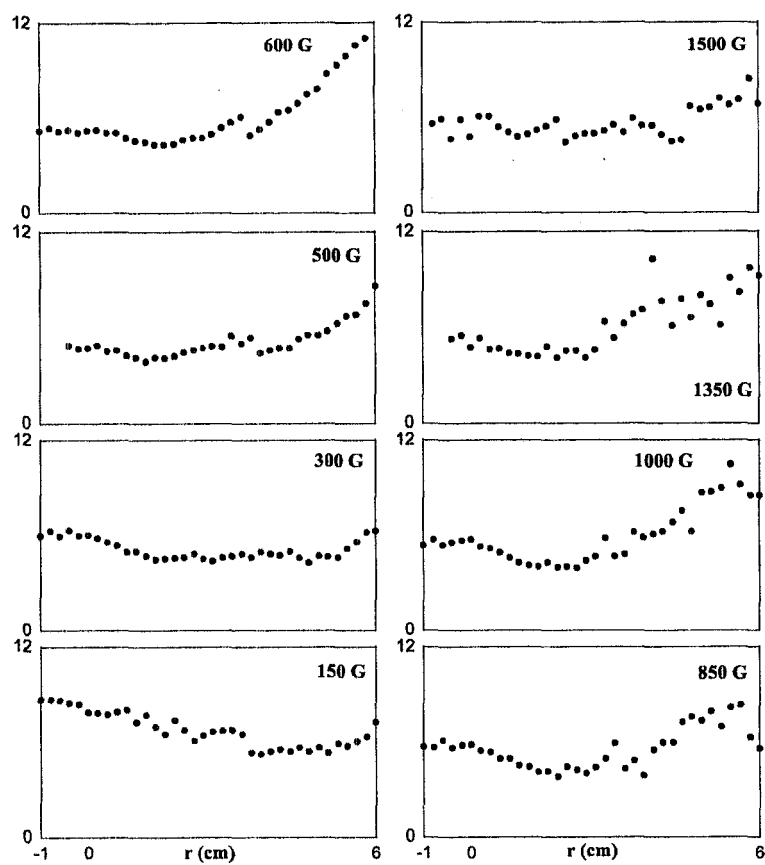


Fig. 13

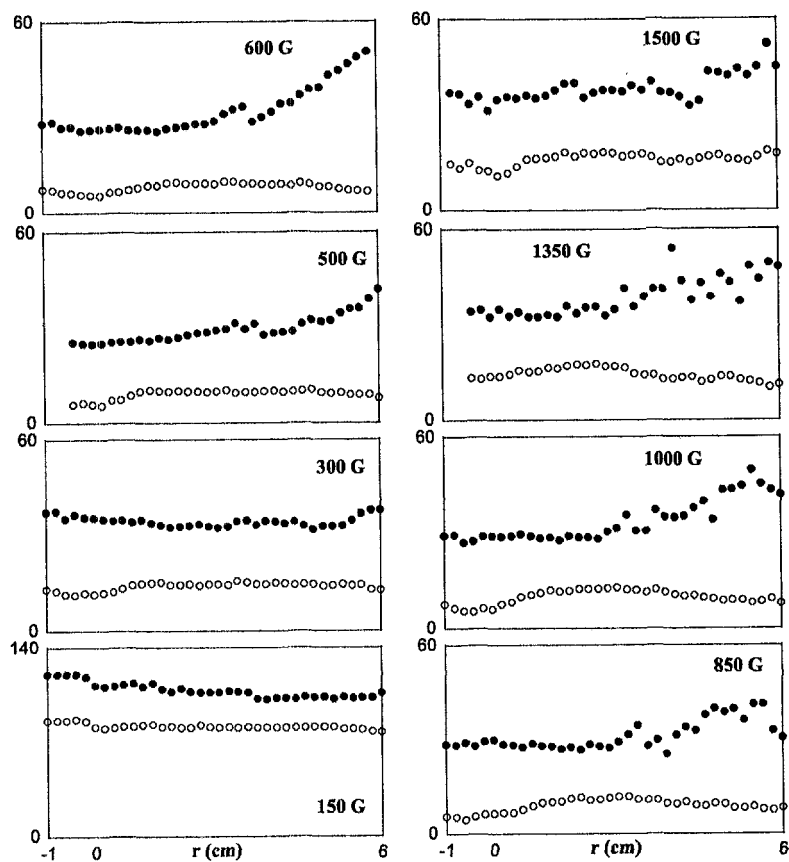


Fig. 14

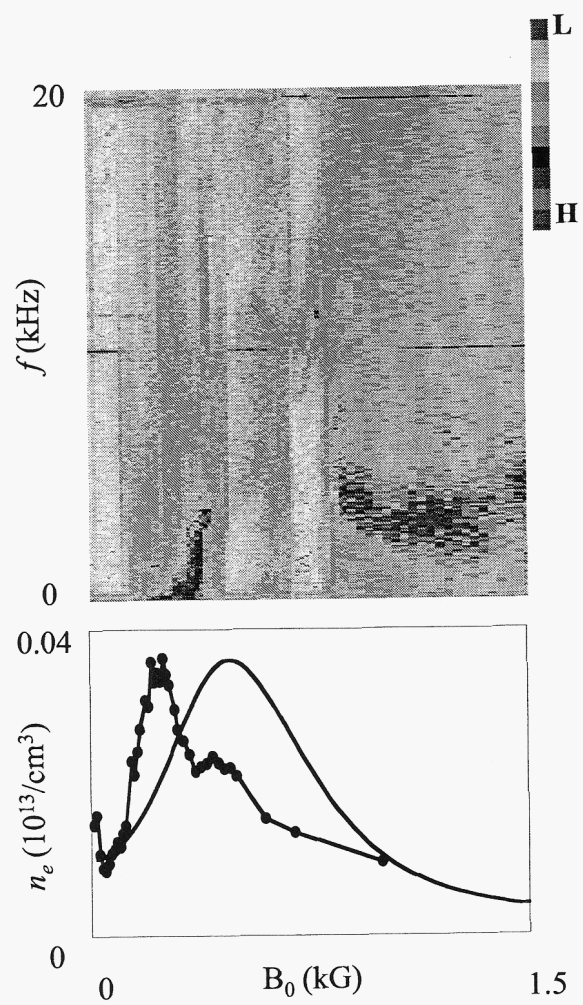


Fig. 15

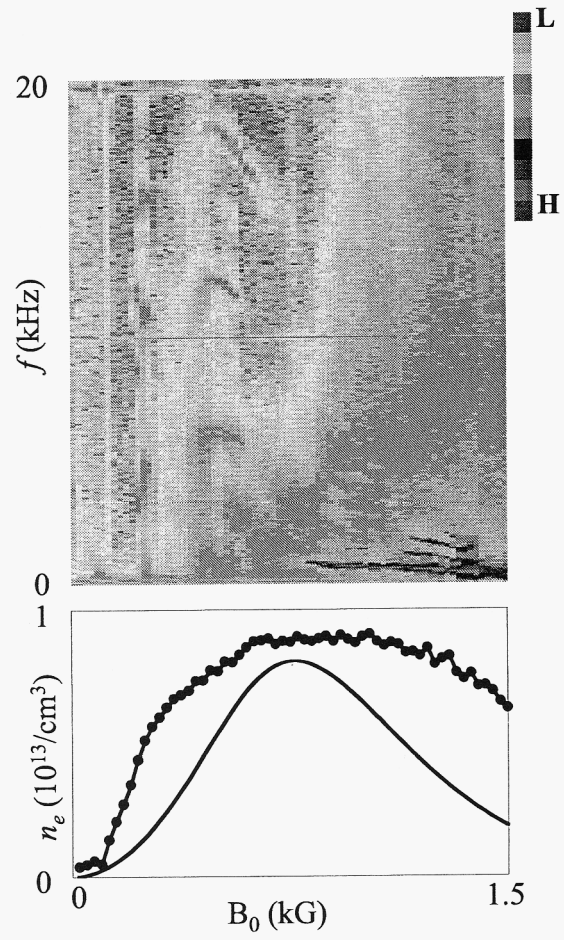


Fig. 16

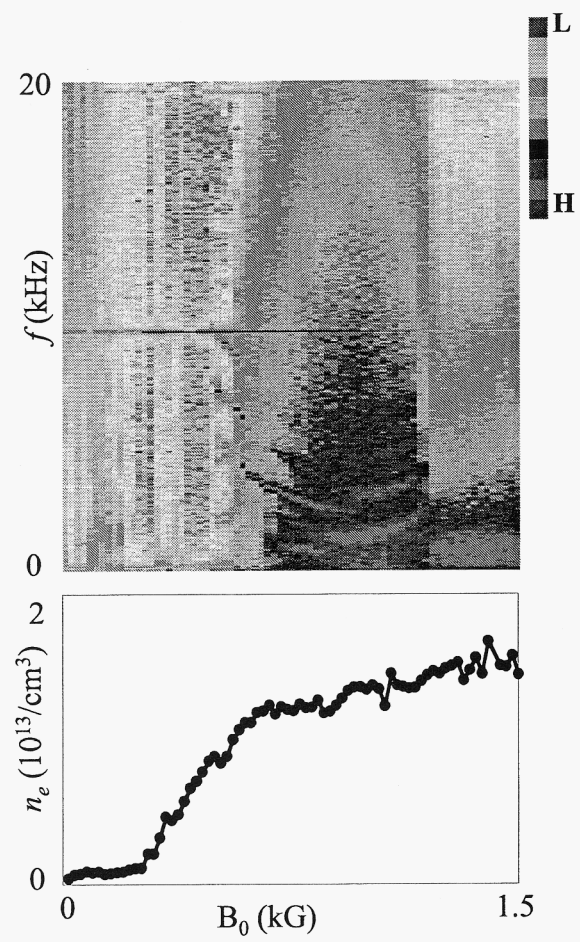


Fig. 17

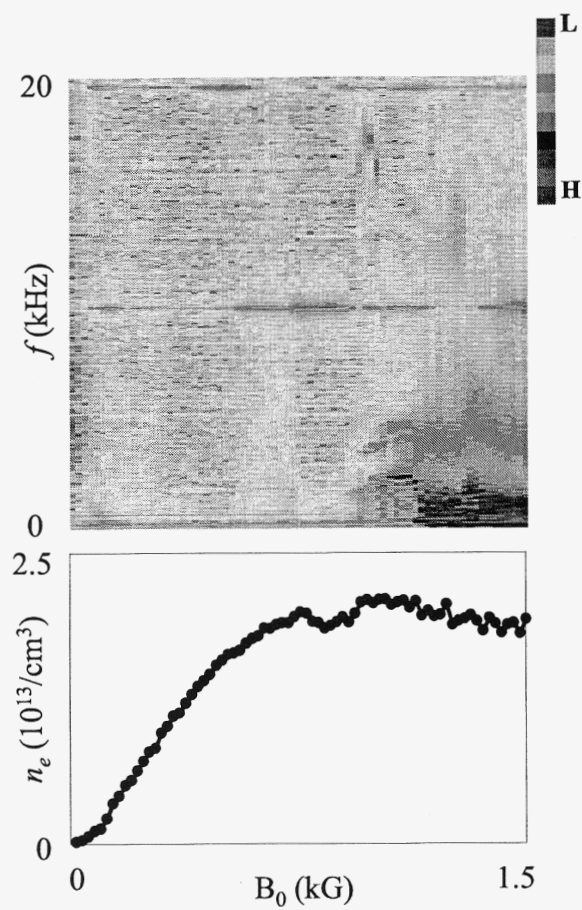


Fig. 18

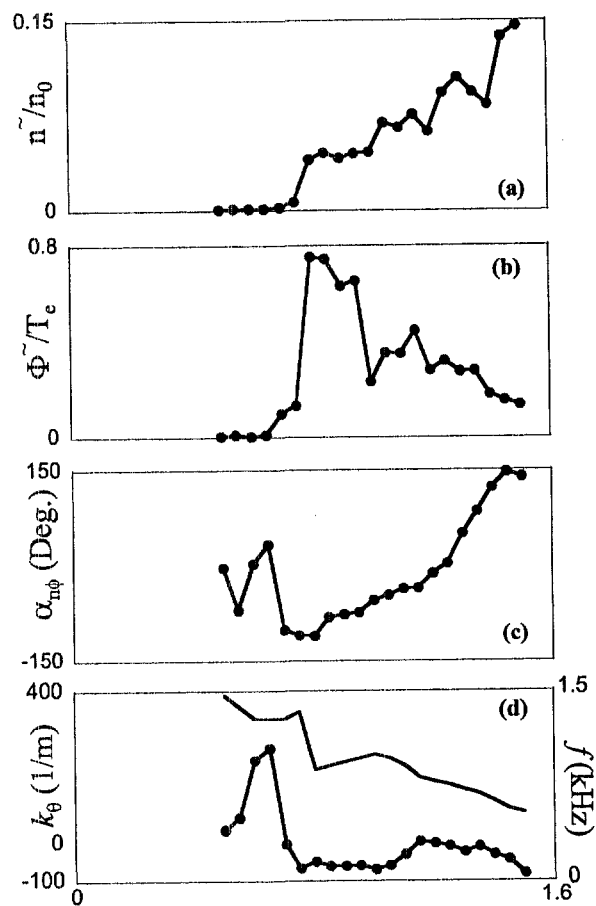


Fig. 19

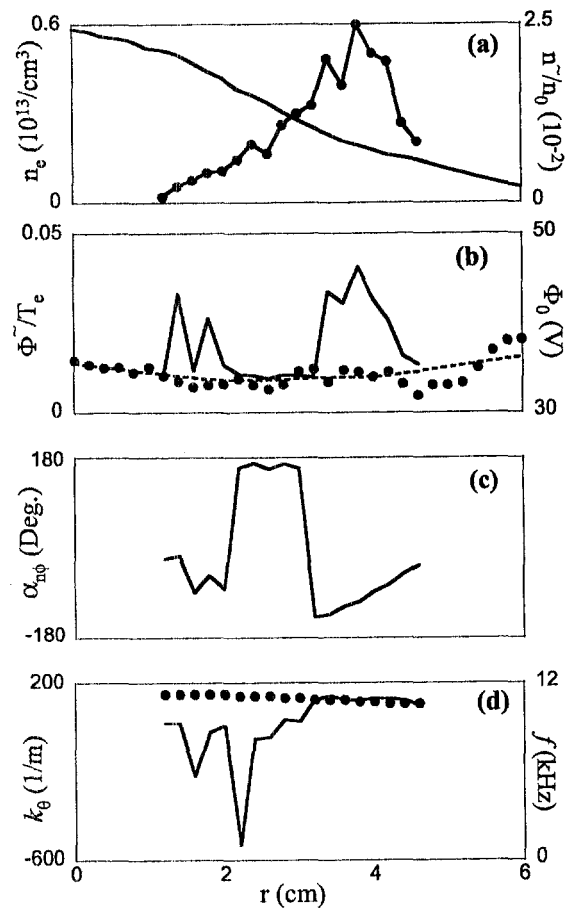


Fig. 20

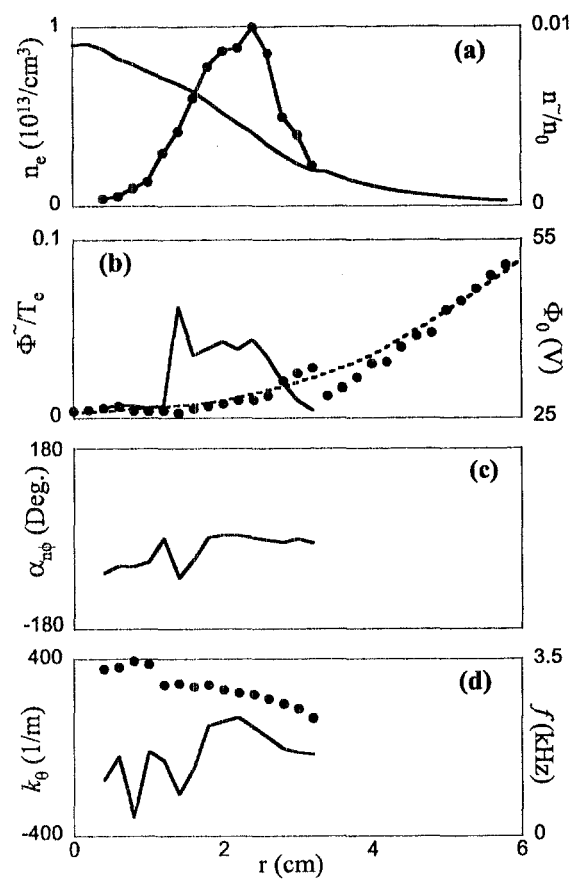


Fig. 21

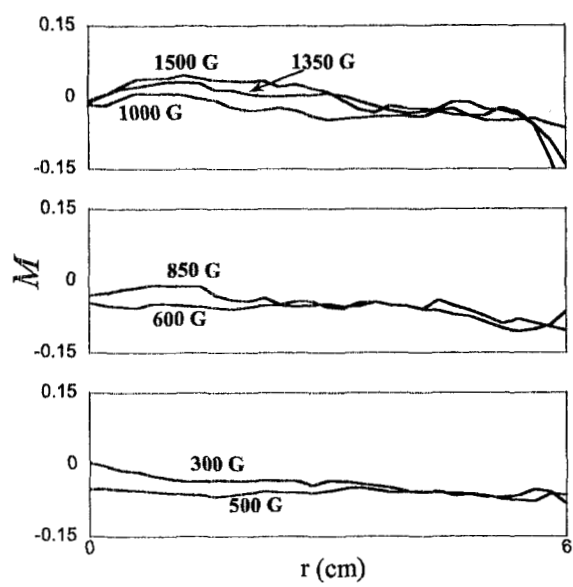


Fig. 22

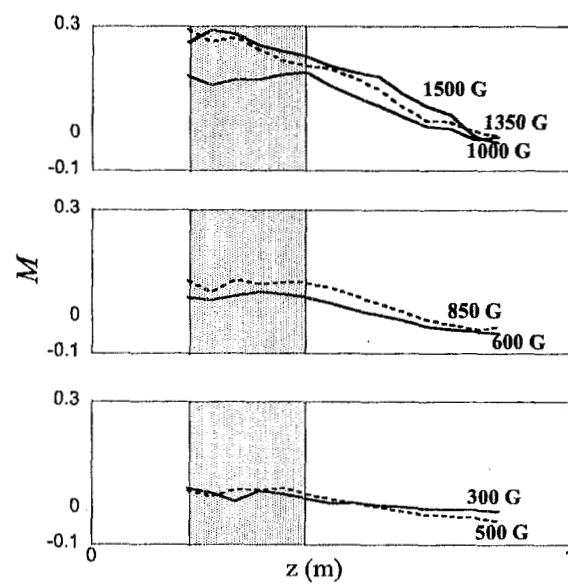


Fig. 23

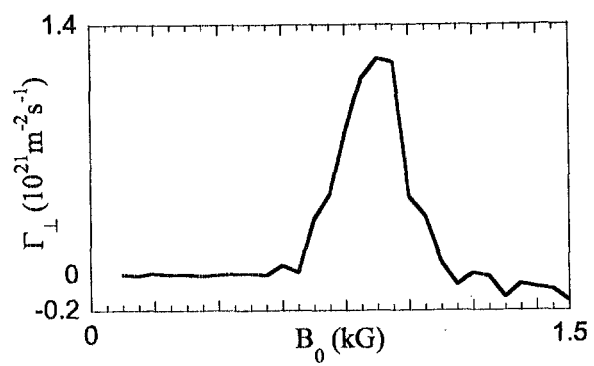


Fig. 24

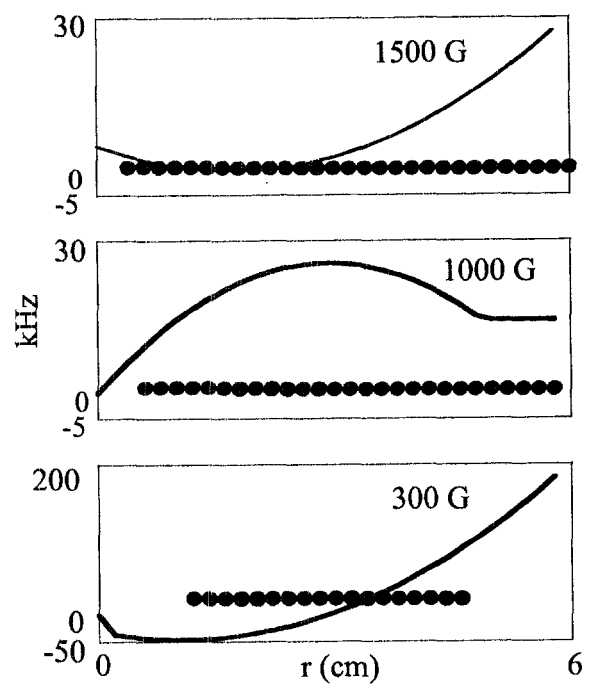


Fig. 25

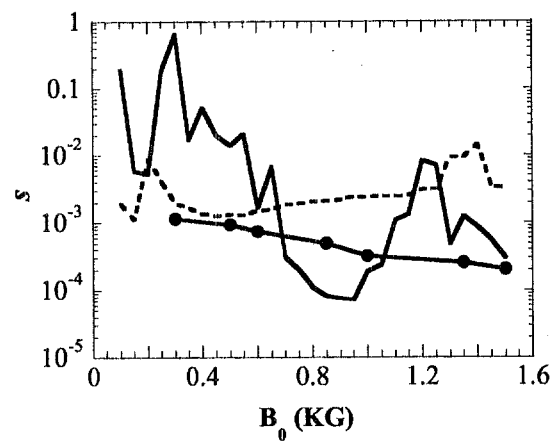


Fig. 26